Supporting Information

to

Theory for nonlinear conductivity switching in semiconducting organic ferroelectrics

Till Johann[1], Weiwei Xie[2,3], Sara Roosta[2], Marcus Elstner[2,4], Martijn Kemerink[1]

1) Institute for Molecular Systems Engineering and Advanced Materials, Heidelberg University, Im Neuenheimer Feld 225, 69120 Heidelberg, Germany.

2) Institute of Physical Chemistry (IPC), Karlsruhe Institute of Technology, 76131 Karlsruhe, Germany.

3) Key Laboratory of Advanced Energy Materials Chemistry (Ministry of Education), State Key Laboratory of Advanced Chemical Power Sources, College of Chemistry, Nankai University, Tianjin 300071, China.

4) Institute of Nanotechnology, Karlsruhe Institute of Technology (KIT), 76344 Eggenstein-Leopoldshafen, Germany.

Contents

1- Ferroelectric ground state preparation

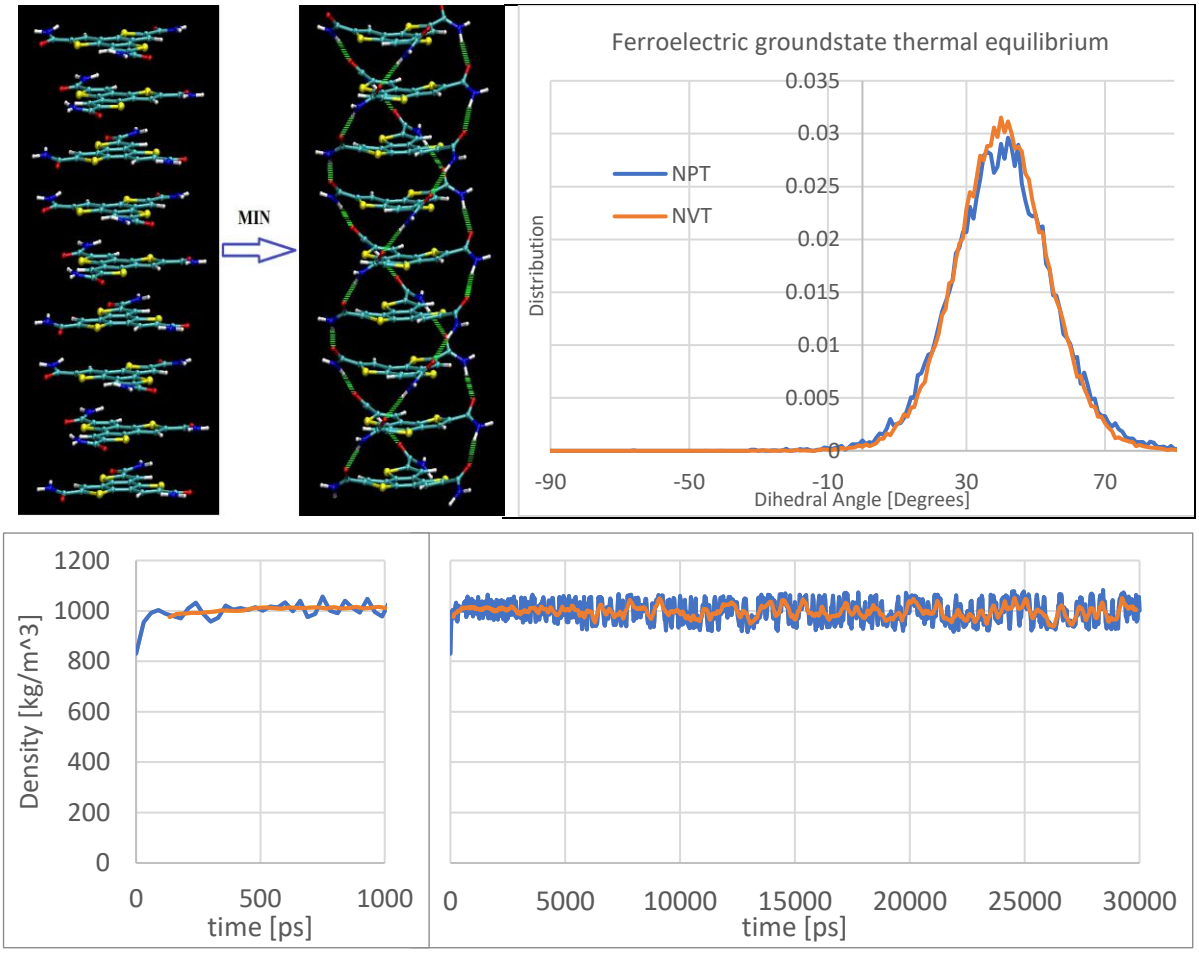

Figure S1: a) Energy minimization is used to prepare the hydrogen-bonded triple helix polarized ground state; b) Dihedral distribution after the system reaches thermal equilibrium in the NVT or NPT ensemble. c) Density of the BTTTA system (9 molecules/column) during NPT, showing a rapid initial increase, followed by fluctuations around an equilibrium value of ~1000 kg/m^3. The blue and orange lines are the raw data and a running average, respectively.

In the NPT simulation, the Gromacs simulation box does change its dimensions (lengths of the 3 axes) while keeping the angles between the basis vectors at 90°, 90° and 60°, which causes a hexagonal structure. Importantly, the exact 'lattice' structure of this type of liquid crystal is of secondary importance to the ferroelectric and charge transfer properties, because the intracolumn interactions are much stronger than the intercolumn ones, due to the long aliphatic tails. To validate this, we performed simulations with different simulation parameters, such as:

NPT, which causes the volume of the box to shrink during equilibration when the initial box volume (set at 9.64nm × 8.35nm × 3.15nm, containing 20304 atoms) is too large; NVT, which causes columns to separate non-uniformly for the same starting condition; simulations with only 6 carbons on the aliphatic tails, which causes the intercolumn distance to be smaller; cubic simulation box, which changes the angle between adjacent columns; MD simulations with 18 and 27 molecules, which showed similar results despite a somewhat larger propensity to form structural defects, especially after ferroelectric switching.

In all of these different scenarios, we could observe a stable H-bonding network. We did not test ferroelectric switching in every single case, but in the cases where we did, it could also be observed. This confirms that the most important property of the system is its H-bonding triple helix and it is this helix structure that dominates the ferroelectric behavior of the system. We also note that the procedure of creating the box was the same procedure as for the BTA calculations, vide infra, for which we saw that results from another publication could be reproduced.

2- Benchmark testing: BTA

The BTA molecule has been studied by MD methods already, which serves as a benchmark for our results.[1] In BTA, there are two possible ways to go from the 3:0 (polarization along +*z*) to the 0:3 (polarization along -*z*) mode. The first is each dihedral angle making a 180° rotation from 40° to -140°. This process leaves the chirality or handedness of the H-bonding network invariant. The other option is for each dipole to invert only its z-component, with the dihedral angle going from 40° to -40°. In this flip, every dipole has to bond with a different bonding partner then before. It inverts the chirality of the H-bonding network. In Ref. [1] it was found that BTA remains in the 3:0 state for fields smaller than 0.22 V/nm and starts making z-flips for stronger fields. The flipping mode will therefore always be a z-flip, since it required a smaller activation energy than the full flip. The z-flip requires only a rotation of around 80°, which minimizes unfavorable intermediate dipole-dipole interactions. This behavior could exactly be reproduced in our simulation. At 0.22 V/nm some of the columns slowly switch, while for values of 0.38 V/nm most of the columns have switched after 50 ns. Figure S2 below shows the time evolution of three representative dihedral angles during the polarization inversion of a BTA column. At around 12 ns, all the dihedrals of the column switch during about 1 ns. A single flip itself takes a few hundred ps, and goes from 40° to -40°, thus performing the z-flip. We find that all BTA columns undergo this z-flip in our simulations.

BTA also possesses another equilibrium H-bonding network, the ferrielectric 2:1 state. Switching this state into the 0:3 configuration occurred at slightly higher fields, and involved a flip of two dihedrals from 40° to -40° and one from -140° to -40°, c.f. Fig. S3, just as observed in Ref. [1]. We note that the molecular cores of BTA remain static during the flip; only the amide groups rotate, which is possible because of the 60° axial rotation between neighboring molecules that provides each amide unit with two equivalent bonding partners (at $\pm$60°) in each neighboring molecule.

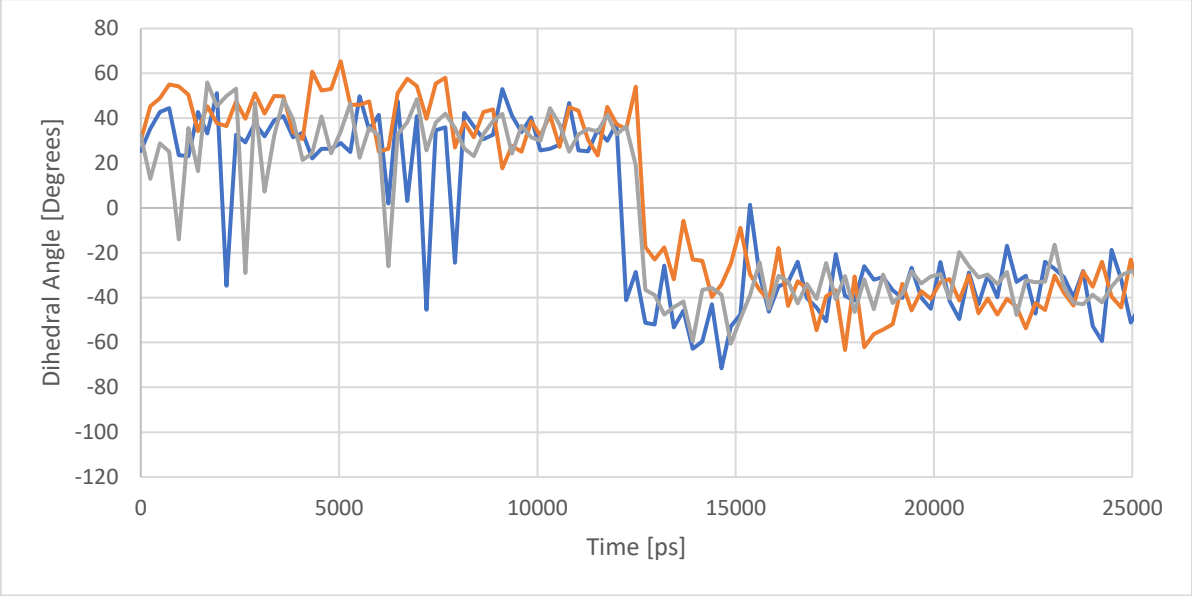

Figure S2: Dihedral dynamics of the amide groups of BTA molecules. Two dihedrals of molecule 42 and one dihedral of the adjacent molecule 43 are shown. They all switch at around the same time, due to the strong dipole-dipole interaction. At around 7 ns, a strong fluctuation of one of the dihedrals occurs, but it is not yet enough to drive the system out of the local minimum.

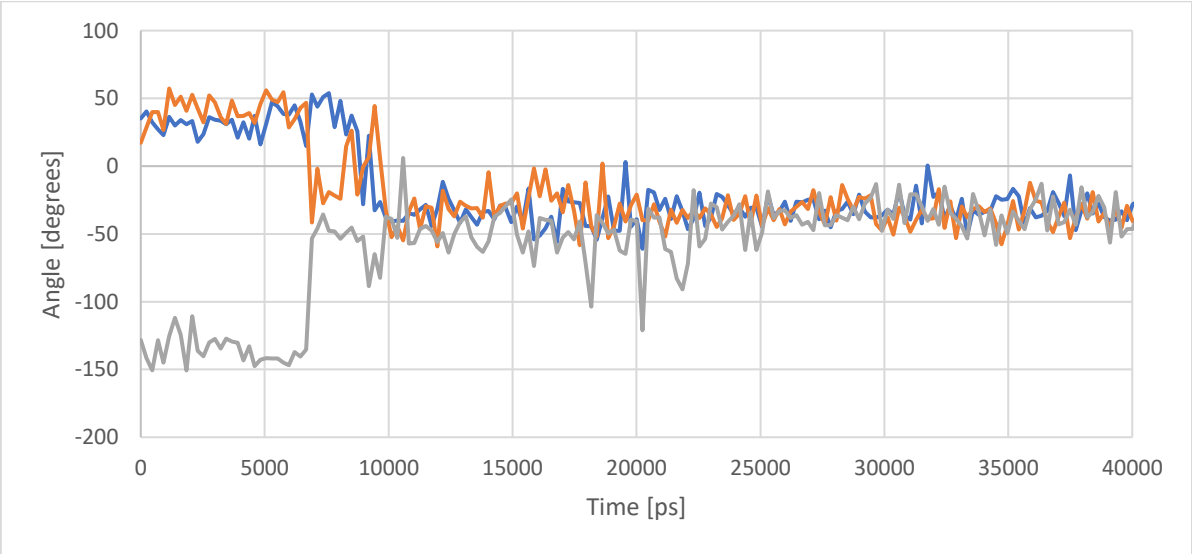

Figure S3: Dihedral dynamics of the three amide groups of BTA molecules, for the flipping mode 2:1 → 0:3.

3- Analysis of ferroelectric switching in BTTTA

In this section, we investigate some of the ferroelectric properties of the simulated BTTTA liquid crystal, with reference to observables that are usually considered in experiments on systems like this. We found that the MD-calculated behavior of BTTTA can be understood in terms of analytical models that are widely used in the framework of ferroelectrics, particularly the Merz Law

$$\tau = \tau_\infty \exp\left(\frac{E_a}{E}\right)$$

and the thermally activated - nucleation limited switching (TANLS) model

$$E_c = \frac{w_b}{P_s} - \frac{k_B T}{P_s V^*} \ln(\nu_0 t / \ln(2)).$$

The following data was obtained from MD simulations with the BTTTA-C12 component, with 8 molecules per column and a 4×4 column crystal grid. The liquid crystal was first energy minimized and thermally equilibrated at T = 300K in an NPT ensemble in the negatively polarized state, and then subjected to different variants of simulations as explained in the following.

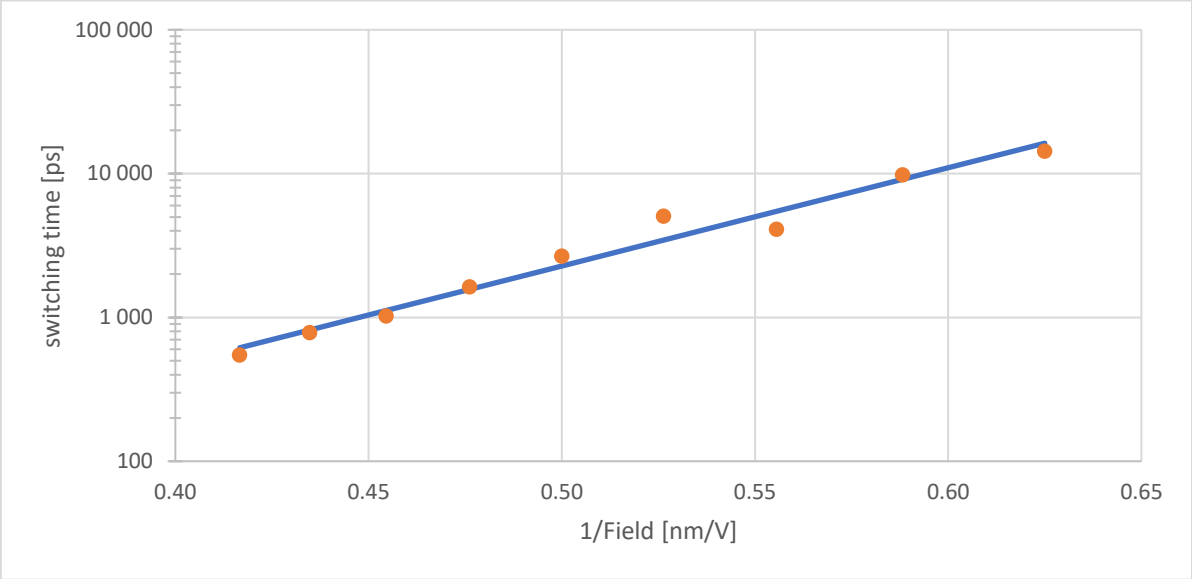

Figure S4: Switching time vs. applied field. At $t = 0$, the system was subjected to a positive electric field, which causes the dipoles to flip up. Multiple simulations at different field strengths were performed. For each simulation, the resulting dipole moment as function of time was fitted to the KAI model $\Delta P(t) = 2P_r\left(1 - \exp\left[\left(\frac{t}{\tau}\right)^d\right]\right)$. The symbols show the fitted switching time τ as a function of the applied field. The switching time as function of field is then fitted by the Merz law $\tau = \tau_\infty \, exp(E_0/E)$ as solid line, obtaining the fit parameters $\tau_\infty = 0.88$ ps and $E_0 = 15.72$ V/nm. The parameter τ_∞ is then used as the inverse attempt frequency $\nu_0 = 1/\tau_\infty$.

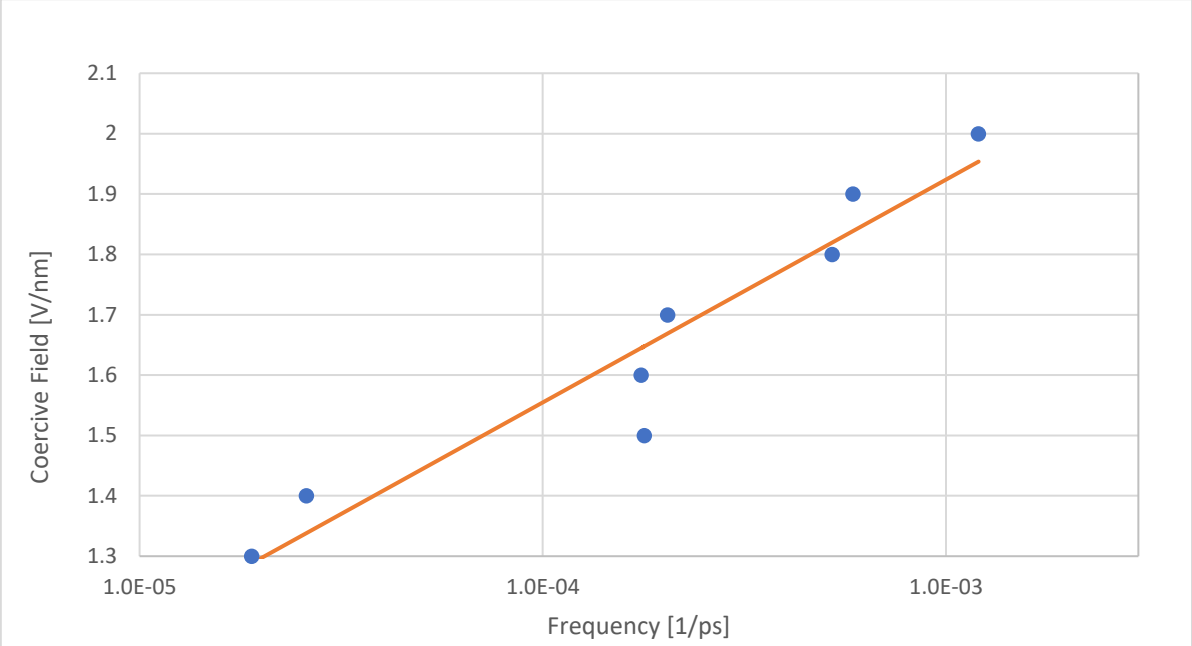

Figure S5: Frequency dependency of the coercive field, fitted with the TANLS model (solid line). Simulations with different applied field strengths (y-axis) were performed. In each of those simulations, we read off the time it takes for the polarization to reach zero. The reciprocal of this time is plotted (symbols) on the x-axis and is the frequency for which the corresponding field is the coercive field. Using $P_s = \frac{960D}{210nm^3} = 15.1 \frac{mC}{m^2}$ and $nu_0 = 1/0.88Thz$ as inputs, we can fit $w_b = 0.29\ eV/nm\text{^}3, V^* = 1.65\ nm^3$ (line) from this frequency dependence of the coercive field.

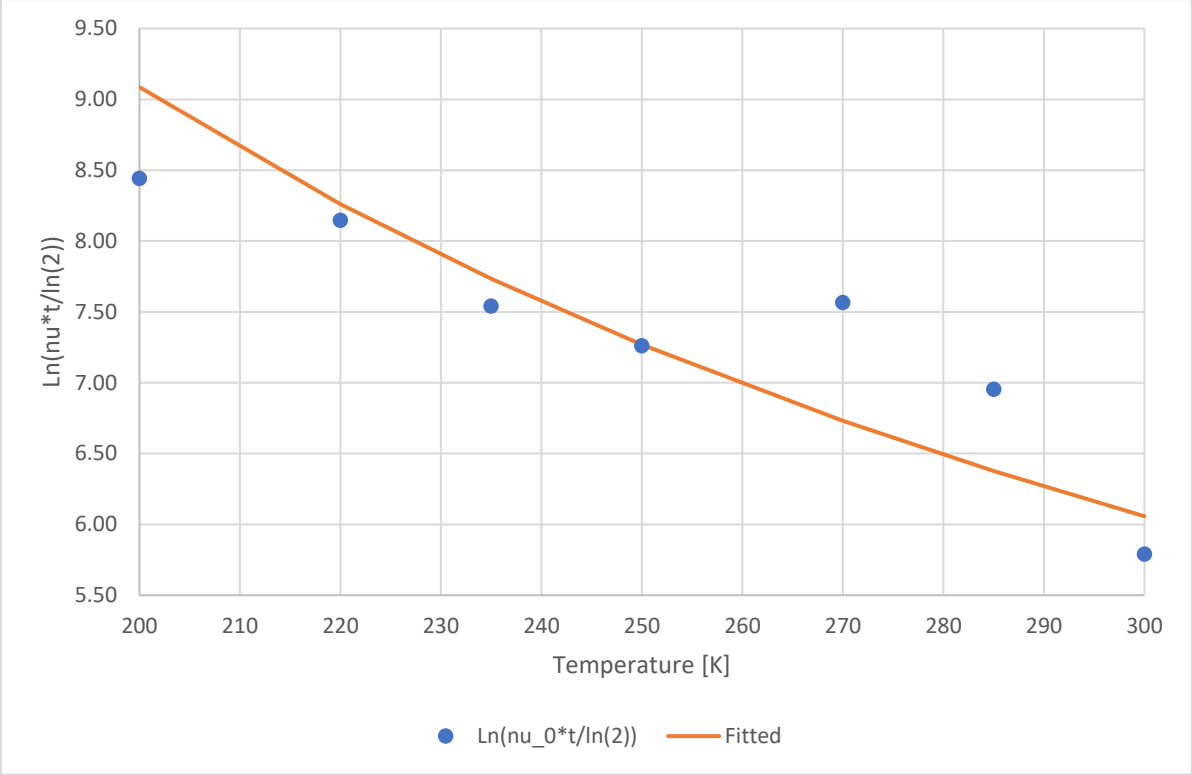

Figure S6: Temperature dependence of the coercive field, fitted with the TANLS model (solid line). A constant electric field of E = 2.2 V/nm was applied, and simulations at different temperatures T are performed. We then read off the time t it takes for the polarization to reach zero for each of the different temperatures, and fit the functional dependence of t vs. T in the TANLS model as $\ln(\nu_0 t/\ln(2)) = \frac{P_S V^*}{k_B T}\left(\frac{w_b}{P_S} - E\right)$. Using the known values for $P_S, k_B T, E$ and V^* from the frequency fit as well as ν_0 from the Merz fit, we can fit the energy barrier $w_b = 0.30\ eV/nm^3$. This value agrees with the value from the frequency dependence fit, demonstrating internal consistency.

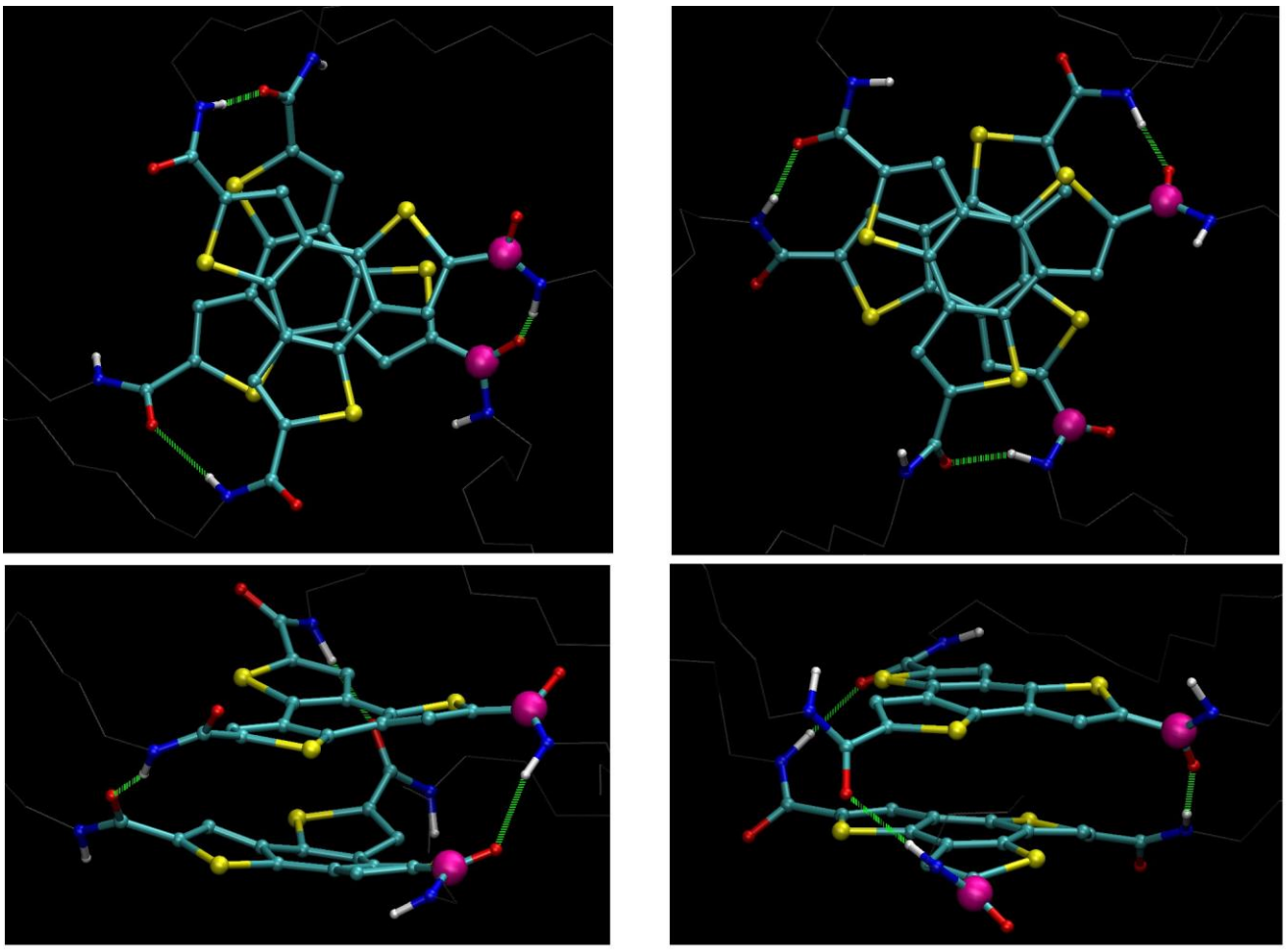

Figure S7: Top (upper panels) and side (lower) views of two molecules in the BTTTA-C12 system. Left: Initial configuration. Two carbon atoms at the amide group are highlighted in pink. Before the switch, these two amides of adjacent molecules lie close to each other and are connected through a H-bond. Right: Final configuration after the switch. The two previously close amide groups have now separated because the molecular cores have twisted with respect to each other. This leads to a change in the H-bonding partners and reverses the handedness of the network.

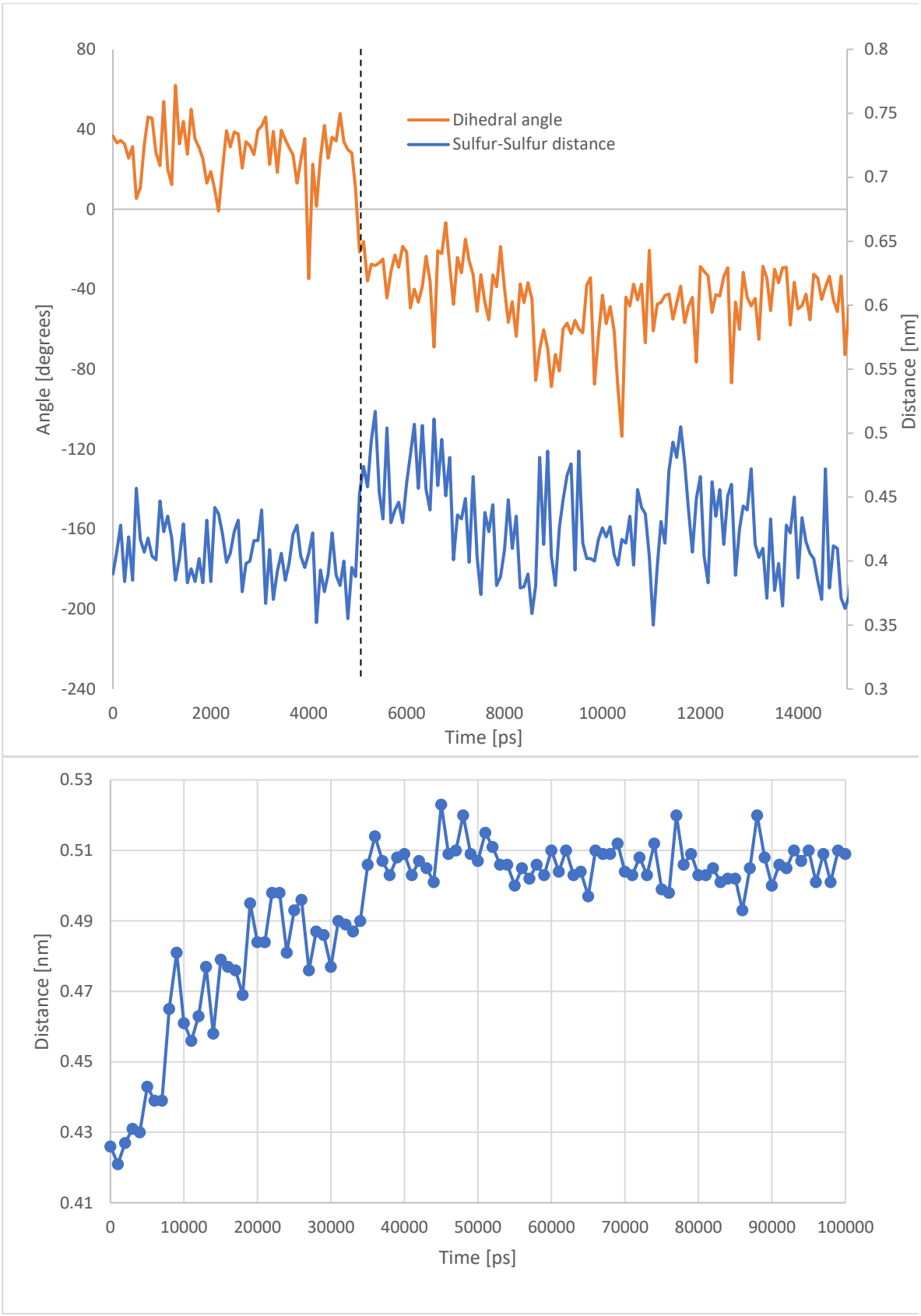

Figure S8: Top) Dihedral angle of an individual amide group and distance between the sulfur atom close to this group, and the corresponding sulfur atom of the neighboring molecule. The polarization reversal at 5000 ps, (black dashed line) in BTTTA is correlated with quick change in

geometry. Bottom) Sulfur-sulfur distances for initially nearest neighbor sulfur atoms during the switching process, averaged over one column of 9 molecules. Initially close sulfur atoms separate to accommodate the formation of a new H-bonding network for a z-flip. In both plots, the structure was originally prepared with negative polarization and is subjected to a constant electric field of E = 1.5 V/nm at t = 0.

Note that the jump at 5000 ps in Figure S8(top) is just an initial reaction of the system. The complete geometrical reorganization process takes several tens of ns. Once the switch is initiated, the column has to perform significant structural reorganizations to accommodate the formation of a new H-bonding network, which is visible as a steady increase in the S-S pair distances.

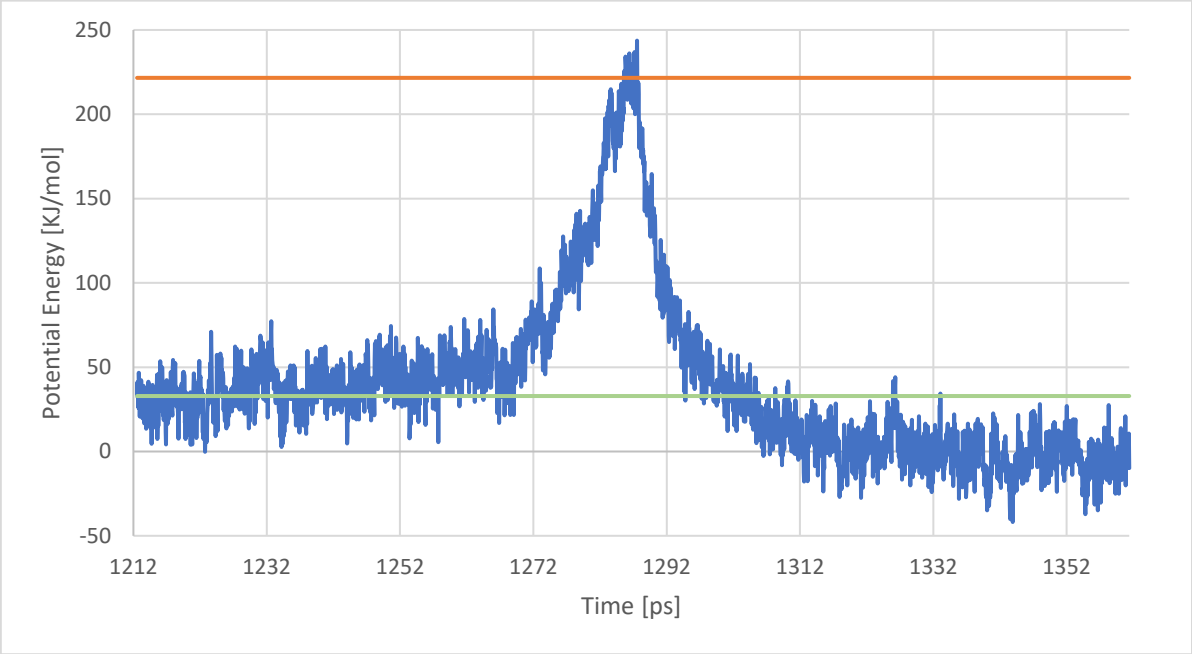

Figure S9: Gromacs forcefield potential energy during a polarization reversal, averaged over 17 simulations of the C0 system. The difference between the green and red lines quantifies the energy barrier for polarization reversal that corresponds to an energy density of w_b = 0.15 eV/nm^3.

4- Details of charge transfer calculations

In the following, we will show and discuss observed properties of the excess charge carrier in the BTTTA environment. All quantum mechanical simulations were performed by using the NPT-equilibrated BTTTA crystal structure as a starting point. This structure was further run for 100ns in the NPT ensemble, taking geometrical snapshots every 0.33 ns, resulting in 300 structurally different initial conditions for the CT simulations, with 16 different columns each. We employ the common QM/MM separation, by restricting the Hilbert space to an individual column and the frontier molecular orbitals, as mentioned in the main text. Additionally, for each individual molecule, the aliphatic chains are removed from the QM zone, since those are negligibly occupied. To assure validity the QM/MM scheme, we took the following steps:

- First, we checked the split between the zones, meaning that the Hilbert space is reduced to the core of the molecules. This was validated by considering the charge density on the tails with the DFTB program. For the frontier MOs, no significant charge population can be found on the tails.
- The link atom approach was used to cap the QM regions with a hydrogen atom. Link atoms are handled using Gromacs´ virtual interaction site features. The goal of this is to exclude the aliphatic tail from the QM zone, but to include the dipolar amide group, in order to properly model the coupling between the dipole moment and charge transfer. More details about this approach and the QM MM coupling can be found in Refs. [2] and [3].
- Finite size effects could be excluded because the MSD (Fig. 4) shows a clear drift regime of the charge, and because the center of charge is sufficiently far away from the boundaries of the QM zone.

Two different types of quantum mechanical simulations were conducted. No-movement simulations restrict the excess charge carrier to an individual molecule. On the other hand, the MM environment (including the atoms of the molecule where the charge carrier is located) is allowed to move. This setting allows us to probe “static” properties of the QM system, such as energies and couplings. For the charge transfer itself, a surface hopping approach “BCJFSSH” is employed.[4]

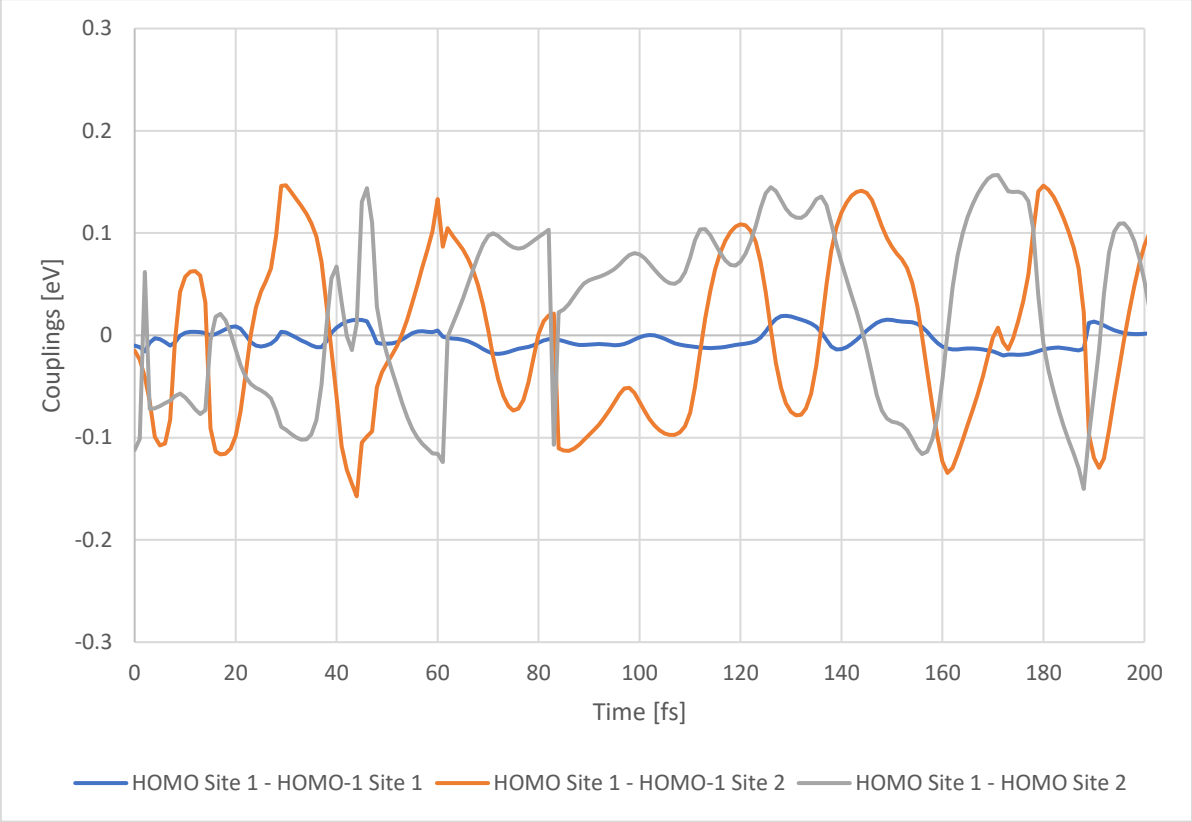

Figure S10: Electron transfer integrals (DFTB Hamiltonian off-diagonal elements) or "couplings", calculated during the no-movement setting. The excess charge carrier is positioned on molecule 1, and we calculate the couplings between the frontier MO's of molecule 1 and its nearest neighbors. As mentioned in the main text, we use the HOMO and HOMO-1 MO's per molecule. The coupling values are very large considering the small experimental mobility, hinting that there must be more macroscopic effects that hinder the charge transport in a real-world material.

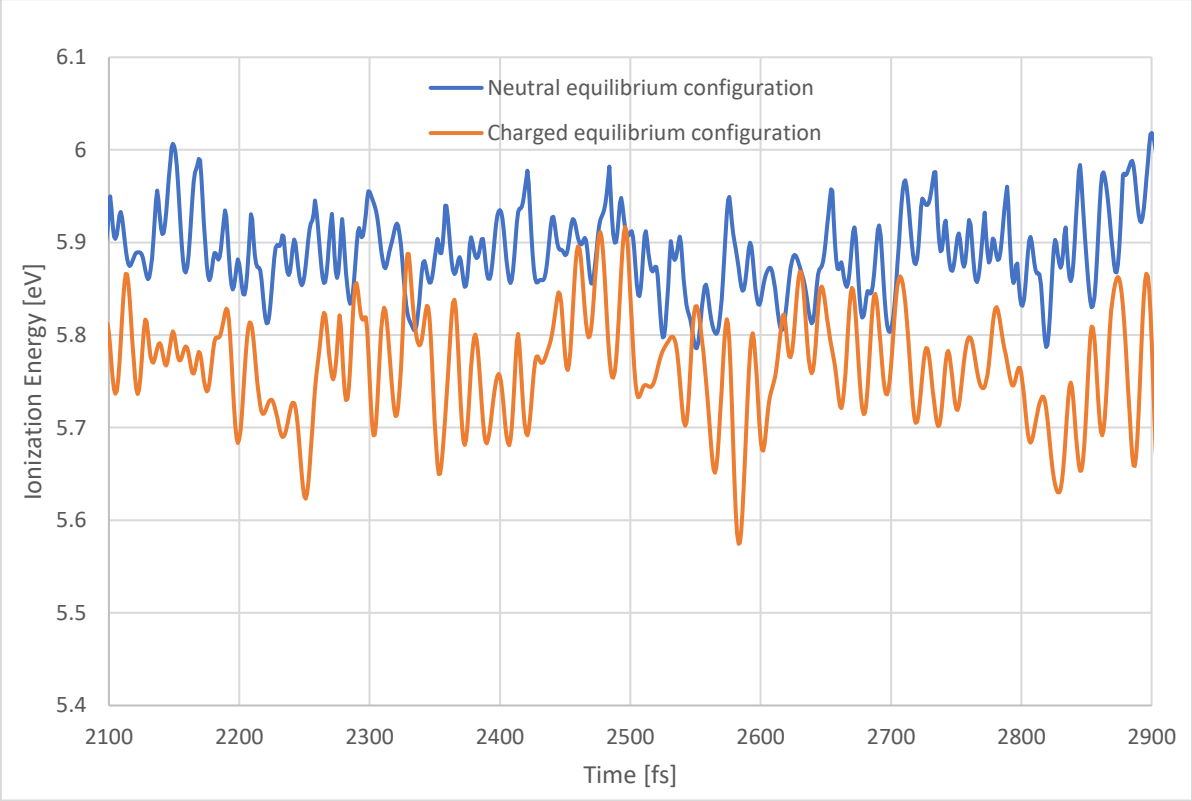

Figure S11: Ionization energies (DFTB Hamiltonian diagonal elements) of the neutral and charged molecular configuration, respectively. As in Fig. S10, the charge carrier is positioned at molecule 1 in the no-movement setting. This leads to intramolecular relaxation and lowers the ionization energy. The difference between the neutral and charged value is the reorganization energy of 0.12eV. This value was benchmarked against a calculation with the Gaussian software, yielding 0.4 eV, which necessitated the use of an implicit relaxation technique as discussed in the main text.

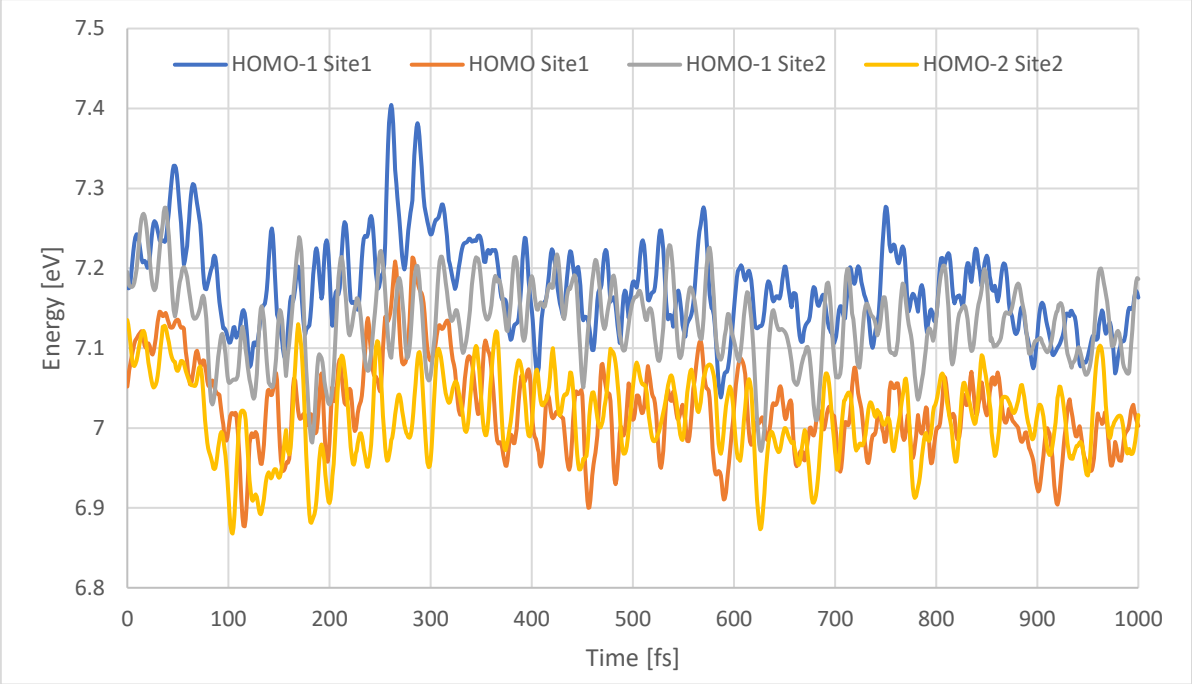

Figure S12: Energies of the frontier MO in the no-movement setting. Additionally, intramolecular relaxation is forbidden, which allows to compare the energies of two fragments without the influence of reorganization. The electrostatic field (or generally the presence of the crystal structure) lifts the degeneracy of HOMO and HOMO-1.

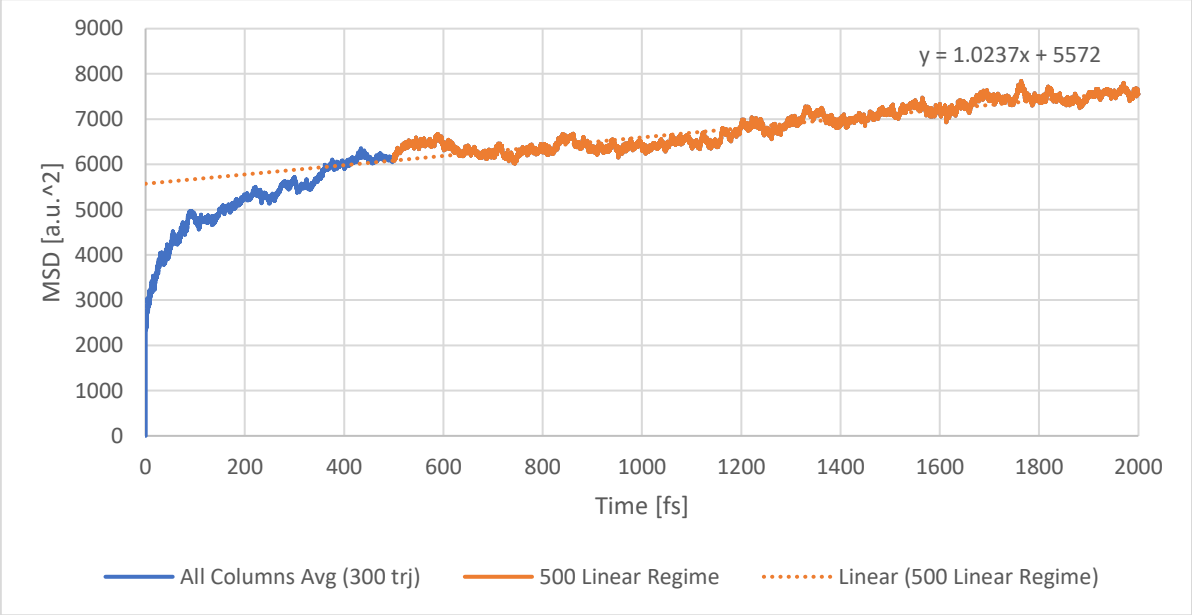

Figure S13: Mean-square-displacement (MSD) of the hole wavefunction during the NAMD simulation without external field, averaged over 15 columns with 20 trajectories each. After an initial thermalization process, the motion enters the diffusive regime where the MSD grows approximately linearly, corresponding to an average zero-field mobility of $\mu_0 = 0.5 \pm 0.1$ cm^2/Vs.

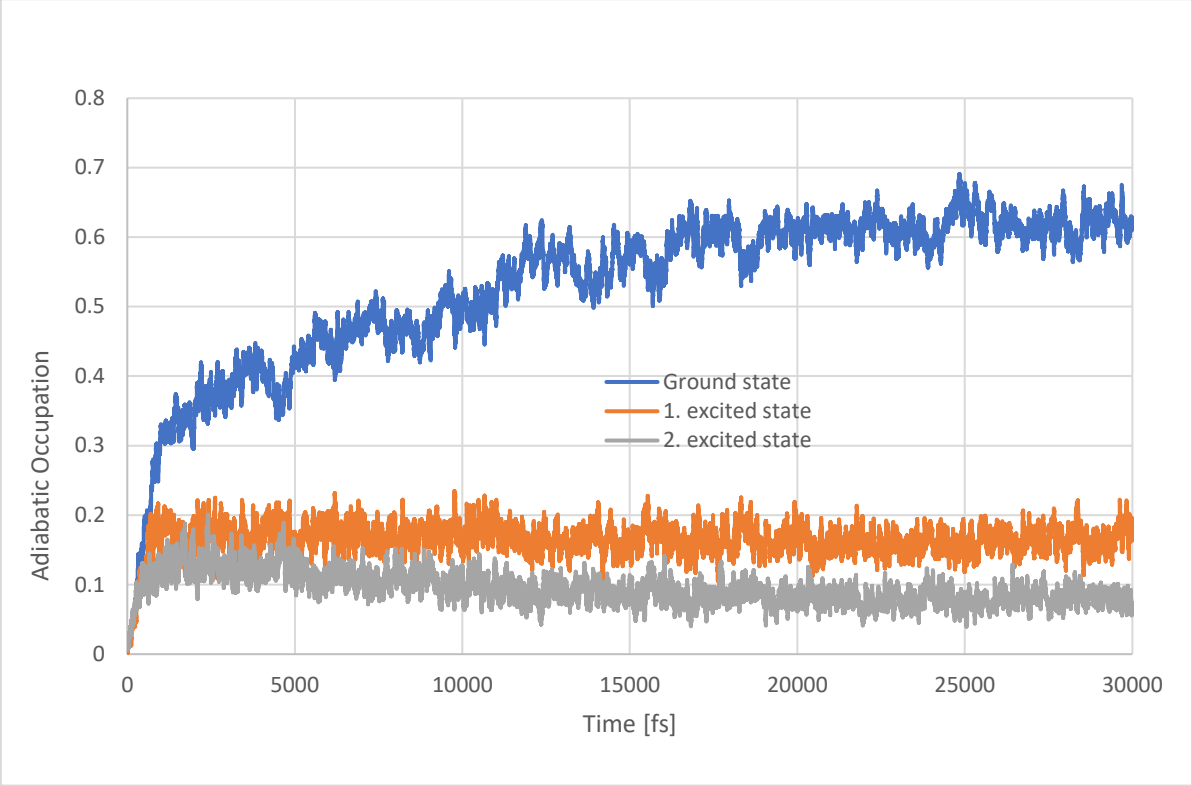

Figure S14: Adiabatic occupation dynamics averages with externally applied field. At $t = 0$, the excess charge carrier is localized at the molecule on the edge of the BTTTA column and allowed to propagate in the BCJFSSH setting. The figure shows the occupation probability of the adiabatic states, that is, the instantaneous eigenstates of the full DFTB Hamiltonian. There is a quick initial thermalization, followed by a slower process until the system reaches thermal equilibrium.

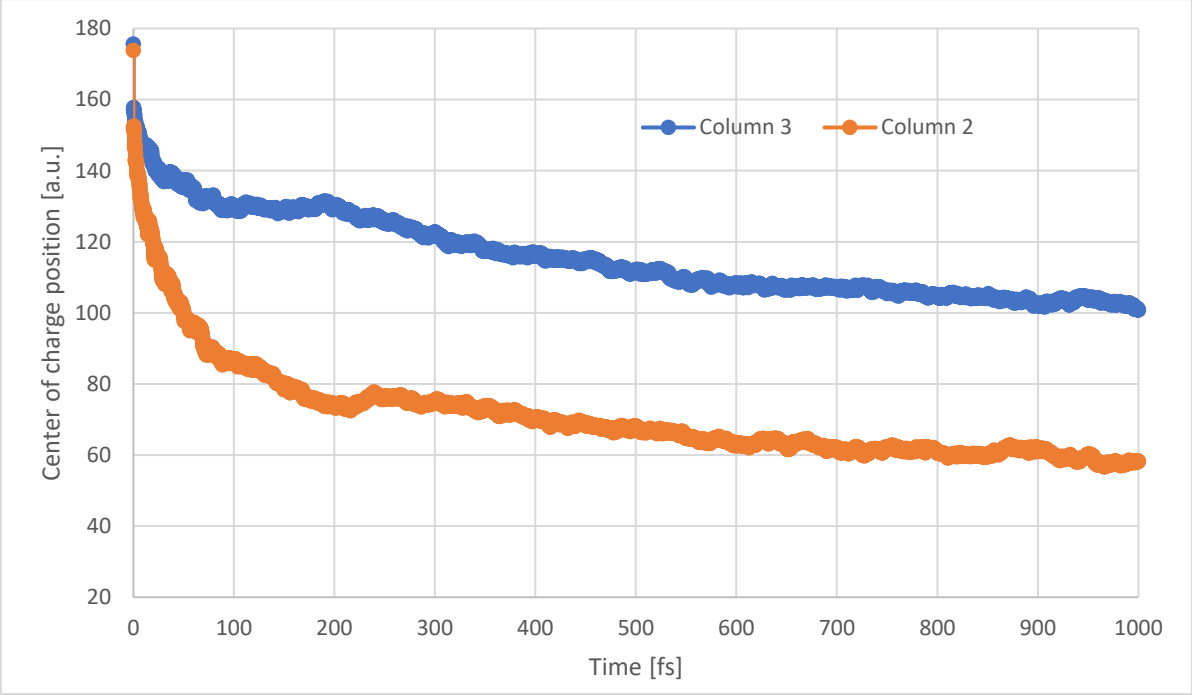

Figure S15: Dynamics of the center of charge of the hole wavefunctions in the presence of an externally applied field. To understand the influence of the columnar geometry on the dynamics of the charge carrier, surface hopping simulations on different columns were performed. An extreme example is shown here in the comparison between columns 2 and 3. The geometrical structure can have a significant effect on the thermalization behavior. In this case, the thermalized mobility is approximately the same.

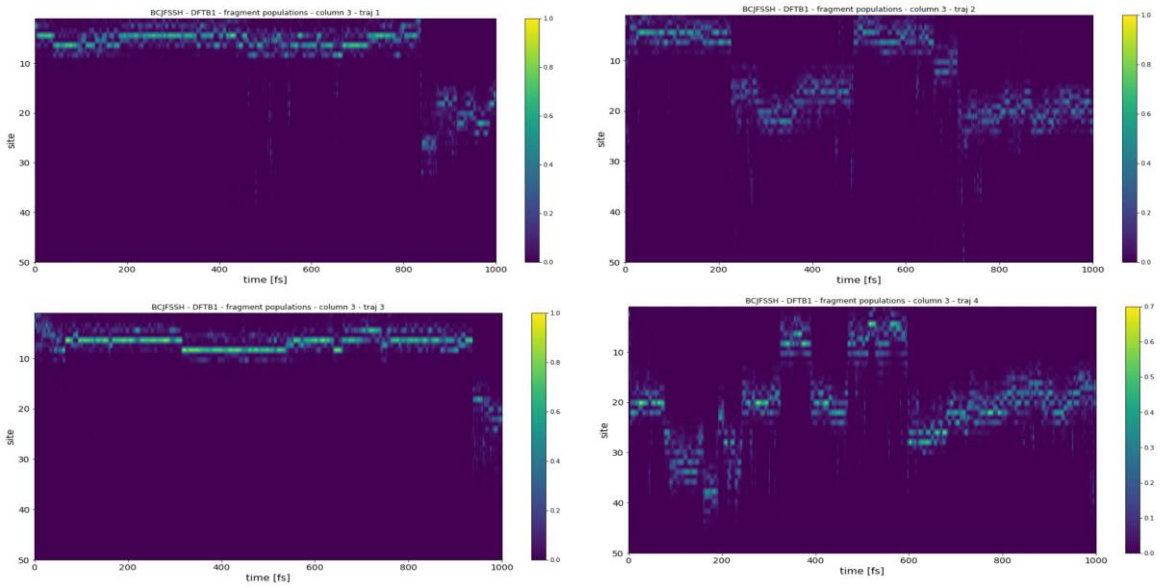

Figure S16: Exemplary CT dynamics in the presence of an applied field. Initially, the charge carrier is positioned at the HOMO of the molecule at the edge of the column and allowed to propagate with the BCJFSSH setting. The figure shows sample trajectories of the dynamics that are then averaged to calculate the mobilities mentioned in the main text.

5 – Supplementary References

(1) Cornelissen, T. D.; Biler, M.; Urbanaviciute, I.; Norman, P.; Linares, M.; Kemerink, M. Kinetic Monte Carlo Simulations of Organic Ferroelectrics. *Phys. Chem. Chem. Phys.* **2019**, *21* (3), 1375–1383. https://doi.org/10.1039/C8CP06716C.

(2) Böser, J.; Kubař, T.; Elstner, M.; Maag, D. Reduction Pathway of Glutaredoxin 1 Investigated with QM/MM Molecular Dynamics Using a Neural Network Correction. *The Journal of Chemical Physics* **2022**, *157* (15), 154104. https://doi.org/10.1063/5.0123089.

(3) Kubař, T.; Elstner, M. Coarse-Grained Time-Dependent Density Functional Simulation of Charge Transfer in Complex Systems: Application to Hole Transfer in DNA. *J. Phys. Chem. B* **2010**, *114* (34), 11221–11240. https://doi.org/10.1021/jp102814p.

(4) Roosta, S.; Ghalami, F.; Elstner, M.; Xie, W. Efficient Surface Hopping Approach for Modeling Charge Transport in Organic Semiconductors. *J. Chem. Theory Comput.* **2022**, *18* (3), 1264–1274. https://doi.org/10.1021/acs.jctc.1c00944.